Confining Potential when a Biopolymer Filament Reptates

Bo Wang,[1] Juan Guan,[1] Stephen M. Anthony,[2] Sung Chul Bae,[1] Kenneth S. Schweizer,[1,2] and Steve Granick[1,2,3]

[1]*Departments of Materials Science and Engineering, University of Illinois, Urbana, Illinois 61801 USA*
[2]*Department of Chemistry, University of Illinois, Urbana, Illinois 61801 USA*
[3]*Department of Physics, University of Illinois, Urbana, Illinois 61801 USA*

Using single-molecule fluorescence imaging, we track Brownian motion perpendicular to the contour of tightly entangled F-actin filaments and extract the confining potential. The chain localization presents a small-displacement Hookean regime followed by a large amplitude regime where the effective restoring force is independent of displacement. The implied heterogeneity characterized by a distribution of tube width is modeled.

　　　　PACS numbers: 47.57.Ng, 83.10.Kn, 87.15.Ya, 87.16.Ka

Polymer entanglement is imperfectly understood [1,2]. This impedes much progress, from processing of plastics to transport in the cell cytoskeleton. Historically, it is modeled [1–3] with increasing sophistication as "reptation" of linear chains within a "tube" along a coarse-grained snakelike "primitive path" [4–7], but too little is known from experiment about the confining potential, a dynamical property that describes transient localization on time scales less than the disentanglement time, owing to the paucity of methods to do so.

Researchers in this field have been well aware of the desirability of this goal. In addition to the voluminous literature comparing models to measurements of mechanical properties and diffusion [6,8], which is indirect, we call attention to the direct measurements. The pioneering work of Sackmann confirmed anisotropy of diffusion for the system that we study here [9], semiflexible filaments of F-actin, but was limited by colloidal bead markers attached to actin. Force measurements were made by dragging DNA through other similar DNA molecules [10] but nonlinear flows complicated interpretation. Computer simulations [6,11] to date are limited to modest degrees of entanglement, $N/N_e \approx 10$ or less (N is the degree of polymerization and N_e the entanglement onset). Here a novel fluorescence approach enables us to quantify distributions of monomer displacement normal to the primitive path for $N/N_e \approx 100$, with subdiffraction resolution. These measurements refer to times far shorter than the disentanglement time, ≈ 100 min for this system [4,11], and thus define a "confining potential" [12].

F-actin networks are chosen since the filaments are long enough to be visualized by fluorescence microscopy [Fig. 1(a)]. The mean filament length (number averaged, L_n) of 23 μm has, from this sample preparation, weight-average to number-average polydispersity, L_w/L_n, of 1.3, and persistence length $\sim$17 μm [13]. Semiflexibility implies that "tube leakage", random looping between discrete entanglements, is unlikely. Subdiffraction spatial resolution is achieved by *sparse* fluorescent labeling.

The experiment begins by mixing trace labeled probe filaments with entangled unlabeled filaments (0.2–2 mg ml^{-1}). Probe filaments are constructed by annealing short segments ($\sim$100 nm long), generated by
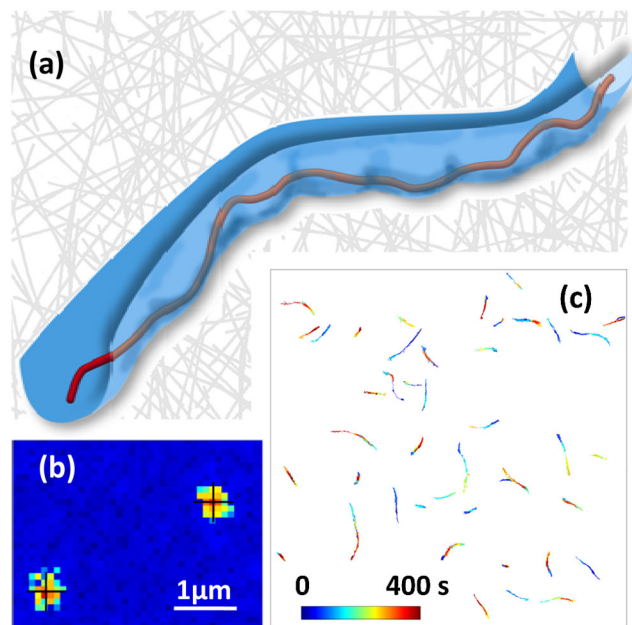

FIG. 1 (color online). The main idea of this experiment. (a) Schematic representation of a chain constrained into a tube-like region by an effective harmonic potential, the collective topological effect of surrounding chains. Minima of this potential define the primitive path. As discussed in the text, the radius of the tube is irregular and polydisperse. (b) A representative image showing two labeled segments of a long actin filament. Analyzing the raw data using a two-dimensional Gaussian spreading function allows one to determine the actual position of segments with subpixel resolution ($\sim$ 10 nm in this set of experiments), indicated by the crosses. (c) An overview of the variety of curvilinearlike diffusive motions of labeled actin segments in entangled F-actin networks. Colors denote time lapse of the trajectory. The F-actin concentration is 0.7 mg-mL^{-1}. Temporal step is 0.5 sec. The dimension of the view is 50 μm $\times$ 50 μm.

passing a mixture of Alexa-568 labeled and unlabeled
F actin at a ratio of 1:10 through a 26 gauge syringe needle
6 times, then fixing the annealed filaments with phalloidin
to prevent treadmilling and depolymerization [14].
Annealing proceeds for >12 h. Brownian motion of
labeled segments was viewed in an epifluorescence micro-
scope with air objective ($63 \times$, NA = 0.75) to focus deep
into the sample (>100 μm) to avoid potential wall effects.
Video images were digitized and analyzed using software
written in house [15]. Local changes in positions of labeled
monomers are resolved with 10 nm precision [Fig. 1(b)].

Representative time traces of fluorescent labels along
F-actin filaments show the expected reptation [Fig. 1(c)].
We identify the primitive path by a B-spline fitting of the
position point cloud using a squared distance minimization
algorithm, and calculate the minimum distance $r_\perp$ from
every measured point to the primitive path with a quadratic
approximation [16]. This one dimensional projection of the
transverse fluctuation distance within the tube brings an
extra experimental uncertainty of <10 nm, estimated from
the variance of a single distance calculated from fitting
with different initial conditions. As the average spacing
between labels along the filaments exceeds the persistence
length, this excludes potential spatial correlations of mea-
sured transverse fluctuations. Chain ends were excluded
from analysis. Trajectories lasting 300–700 sec were ana-
lyzed with a frame rate (0.5 sec) sufficiently slow that
bending fluctuations, which are on the msec time scale
[17], did not contribute. This time scale is longer than the
entanglement time, the time that the movement of the
filaments starts to become sterically confined by their
neighbors [11].

In Fig. 2, histograms of root-mean-squared (RMS) trans-
verse fluctuations, $\sqrt{\langle r_\perp^2 \rangle}$, of single time traces of filaments
are shown for two actin concentrations. The right-skewed
shapes deviate from the classical tube radius notion.

The ensemble-average dynamical confining potential
felt by an actin monomer, $V(r_\perp)$, is extracted by combining
the full trajectories from all filaments using the relation
[9,12]: $\frac{V(r_\perp)}{k_B T} = -\ln\frac{P(r_\perp)}{P(0)}$, where $P(r_\perp)$ is the transverse
distance probability distribution, and $k_B T$ is the thermal
energy. Experimental limitations preclude measurement of
the (expected weak for $N \gg N_e$) time dependence of
$V(r_\perp)$ [12]. Figure 3(a) shows an example of the displace-
ment probability distribution spanning 3 orders of magni-
tude of transverse fluctuation. Data for a single filament
(crosses) agrees with the ensemble-average for many fila-
ments (circles) though the former is noisier, showing that
fluctuation on the single filament level is well represented
by the ensemble distribution. For the first logarithmic
decade of probability distribution, the transverse distance
$r_\perp$ agrees with the classical picture of a harmonic con-
straining potential, following the Gaussian probability dis-
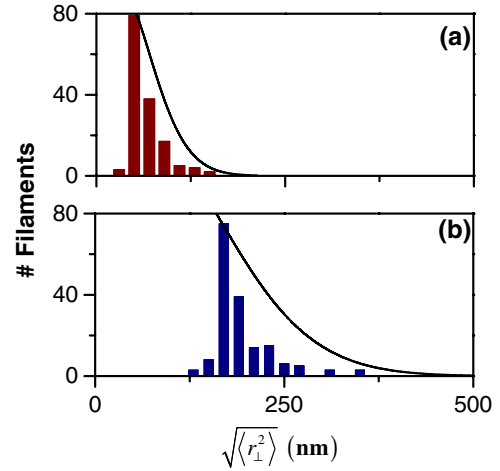tribution $P(r_\perp) \propto \exp(-\frac{r_\perp^2}{R_e^2})$, where R_e is the tube radius

FIG. 2 (color online).   Histograms of RMS transverse fluctua-
tions (distribution of "second moments") of single time traces
along filaments at actin concentrations of 1 (a) and
0.2 mg ml^{-1} (b). The solid lines compare to the expected dis-
tribution predicted by the ensemble-averaged model presented in
the text, assuming that each filament feels a homogenous envi-
ronment. The discrepancy between these two distributions dem-
onstrates that the heterogeneity quantified here occurs on length
scales smaller than the filament length.

defined as the distance beyond which the constraining
potential exceeds $k_B T$. Beyond this, it is better described
by an exponential decay, $P(r_\perp) \propto \exp(-\frac{|r_\perp|}{\lambda})$. This is the
case for probabilities <0.1, corresponding to a constrain-
ing potential of $\sim 2 k_B T$ or more, a regime not probed in
prior studies [9]. At other actin concentrations, the distri-
bution was similar except that it broadened as concentra-
tion decreased. The concentration range studied was
limited by the requirement to achieve entanglement at
the low end and to avoid nematic ordering at the upper
end [18].

Figure 3(b) shows an effective equivalent restoring
force, $-\frac{dV_\perp}{dr_\perp}$, plotted against the transverse distance. For
small displacements, force increases linearly with trans-
verse distance and the spring constant is the slope, as
postulated in classic tube or slip-link models. But in the
large displacement regime, the restoring force is constant
and in the range ~ 10–100 fN, the value depending on actin
concentration. This softening is not included in theories of
polymer dynamics of which we are aware. However, for
these semidilute solutions whose mean concentration is so
small ($\approx 10^{-4}$ in terms of volume fraction for actin) large
concentration fluctuations are present. It is then reasonable
to expect the entangled network, which controls actin
monomer displacements, to have a broad distribution of
physical and mechanical mesh sizes. This we propose is
the origin.

We now introduce a simple physical quantification of
this idea. (i) It is reasonable to model spatial distribution of
filaments as a random fluid of thin rods, since actin con-

centrations are below the nematic phase transition. (ii) Given (i), the physical mesh (ξ) distribution was determined by Ogston to be: $P_\xi(\xi) = 4\pi\rho\xi \exp(-2\pi\rho\xi^2)$, where ρ is the contour length per volume [19]. This implies that the suspension can be thought of as tiling space with meshes (groups of nearby filaments) of variable local density and size randomly distributed. (iii) As in semidilute solutions of entangled flexible chains in a good solvent, a direct connection between physical mesh and entanglement (or localization tube) length applies. Mean field ideas [11] and a binary collision approximation (BCA) [20] show that average tube radius and mesh size are related as: $R_e = a\xi^{6/5}l_p^{-(1/5)}$ where l_P is the persistence length of semiflexible polymer and a is a numerical constant. This concentration dependence of the tube radius has been recently revisited [21,22] but we show below that this simple relation is consistent with our experimental data. The BCA allows us to employ this relation locally, on a mesh-by-mesh basis, in order to relate local spatial variation of actin density to local spatial variation of the tube radius. How correlation effects should be included is unknown, and (as we show) apparently unnecessary to adequately describe our observations. Then the probability a given actin monomer has displacement $r_\perp$ is given by probability density averaged over spatial and temporal fluctuations, $\quad P(r_\perp) = \int d(R_e) P_{R_e}(R_e) \frac{1}{\sqrt{\pi R_e^2}} \exp(-\frac{r_\perp^2}{R_e^2})$, where for each specific tube radius the distribution of transverse fluctuation is Gaussian. The implied distribution of tube radii, $P_{R_e}(R_e)$, is plotted in Fig. 4(a). But the tube radius cannot be arbitrarily small, since filaments have finite size, so a lower limit of integration is introduced. This physical argument generates a dimensionless formulation of the 1D transverse distance distribution

$$P(\tilde{r}_\perp) = c \int_\alpha^\infty d(\tilde{R}_e) \tilde{R}_e^{-(1/3)} \exp\left(-\frac{\pi}{4}\tilde{R}_e^{5/3}\right) \exp\left(-\frac{\tilde{r}_\perp^2}{\tilde{R}_e^2}\right),$$
(1)

where $\bar{R}_e \equiv a(8\rho)^{-(3/5)} l_p^{-(1/5)}$, $\tilde{R}_e \equiv R_e/\bar{R}_e$, $\tilde{r}_\perp \equiv r_\perp/\bar{R}_e$, α is the dimensionless lower cutoff of the integration, and c is a normalization factor depending on $\bar{R}_e$ and α.

For large $r_\perp$, using the method of steepest descent Eq. (1) predicts a nearly exponential tail: $P(r_\perp) \propto e^{-1.2(\frac{r_\perp}{\bar{R}_e})^{10/11}} \approx e^{-(r_\perp/\lambda)}$, where $\lambda \approx \frac{\bar{R}_e}{1.2}$. Physically, the tail is the ensemble-average consequence of an effectively static disorder of harmonic tube constraints which follow the local variation of mesh sizes. This agrees with data at different actin concentrations and suggests [Fig. 3(a)] that $\alpha = 1$. This parameter mainly determines the position of transition from Gaussian to exponential-like distribution. A value of unity implies the mean tube radius [Fig. 4(a)]:

$$\langle R_e \rangle \approx 1.6\bar{R}_e \approx 1.6\rho^{-(3/5)} l_p^{-(1/5)},$$
(2)

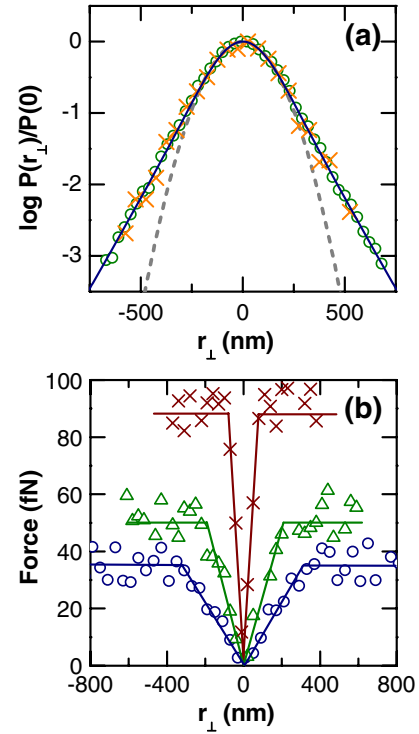where $\bar{R}_e$, effective filament thickness, is plotted logarith-

FIG. 3 (color online). Illustrative transverse fluctuation distributions. (a) Transverse distance probability distributions, plotted against distance normal to the primitive path, for an ensemble of hundreds of filaments (circles) and for the trajectory of a single filament (crosses). Actin concentration is 0.5 mg-mL^{-1}. The solid line is a fit using Eq. (1) with $\alpha = 1$. The dashed line is the corresponding Gaussian fit to the center part of the distribution. (b) Effective restoring forces, inferred from a Boltzmann distribution law as explained in the text, plotted against transverse distance. The actin concentrations are 1 (crosses), 0.5 (triangles), and 0.2 mg ml^{-1} (circles).

mically versus actin concentration in Fig. 4(c), and follows a power law $\bar{R}_e \propto c^{-(3/5)}$, consistent with its definition. Note that the cutoff generates a monotonically decreasing tube radius distribution, consistent with the observation of positive skewness of RMS fluctuations in Fig. 2. To illustrate the connection between the distribution and the mean value, the distribution rescaled by mean tube radius is also plotted in Fig. 4(b). Fast thermal fluctuation of single filaments accounts for concentration dependence of the effective filament thickness, which is defined by the largest possible amplitude of bending fluctuation considering the statistically averaged interfilament interaction. Another plausible physical origin of the cutoff is strong suppression of small meshes due to their high local osmotic pressure and hence large free-energy cost.

The present experiments cannot discriminate between spatial and temporal heterogeneity, which remains as an enticing challenge. Another open question concerns the length scale of heterogeneity. That the distribution of RMS fluctuations from a single filament are narrower
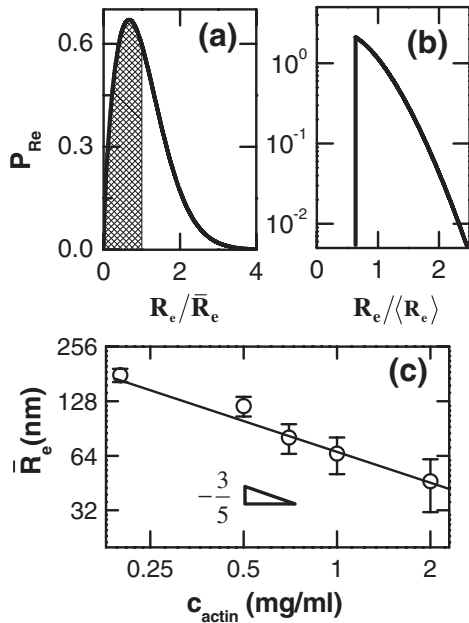
FIG. 4.   The tube radius distribution. (a) The distribution of tube radius, $\bar{R}_e P_{R_e}(\tilde{R}_e) = \frac{5\pi}{12} \tilde{R}_e^{2/3} \exp(-\frac{\pi}{4} \tilde{R}_e^{5/3})$, is plotted against the dimensionless $\tilde{R}_e$ defined in the text, on linear scales. The shadowed region shows the needed lower cutoff determined by fitting the data. (b) The distribution of tube radius plotted on semilogarithmic scales rescaled by mean tube radius, taking lower cutoff into consideration so that the average tube radius $\langle R_e \rangle = 1.6\bar{R}_e$. (c) Logarithmic plot of $\bar{R}_e$ versus actin concentration. The error bars show the standard deviation from many experiments. The solid line has slope $-3/5$.

(Fig. 2) than the theoretically deduced tube radius distribution suggests it to be smaller than the filament length. That is supported by the fact that data for a single actin filament, Fig. 3(a), are consistent with the ensemble average. However, the data do not allow us to distinguish between this and other small scales, the entanglement length and persistence length. Although the microscopic nature of this heterogeneity is not fully understood, we hope these findings will call attention to the prominence of distributions instead of "averaged" numbers, even in classical models [23].

Note added.—Recently, we came across related work [23]. The approach in that paper differs from ours both experimentally and theoretically but the qualitative conclusions are in broad agreement.

[1] D. J. Read, K. Jagannathan, and A. E. Likhtman, Macromolecules **41**, 6843 (2008).
[2] P. G. de Gennes, J. Chem. Phys. **55**, 572 (1971).
[3] M. Doi and S. F. Edwards, *The Theory of Polymer Dynamics* (Clarendon, Oxford, 1986).
[4] J. Käs, H. Strey, and E. Sackmann, Nature (London) **368**, 226 (1994).
[5] T. T. Perkins, D. E. Smith, and S. Chu, Science **264**, 819 (1994).
[6] R. Everaers, S. K. Sukumaran, G. S. Grest, C. Svaneborg, A. Sivasubramanian, and K. Kremer, Science **303**, 823 (2004).
[7] A. Wischnewski, M. Monkenbusch, L. Willner, D. Richter, and G. Kali, Phys. Rev. Lett. **90**, 058302 (2003).
[8] D. C. Morse, Macromolecules **31**, 7044 (1998).
[9] M. A. Dichtl and E. Sackmann, New J. Phys. **1**, 18 (1999).
[10] R. M. Robertson and D. E. Smith, Phys. Rev. Lett. **99**, 126001 (2007).
[11] H. Isambert and A. C. Maggs, Macromolecules **29**, 1036 (1996).
[12] Q. Zhou and R. G. Larson, Macromolecules **39**, 6737 (2006).
[13] L. Limozin, M. Bärmann, and E. Sackmann, Eur. Phys. J. E **10**, 319 (2003).
[14] D. B. Murphy, R. O. Gray, W. A. Grasser, and T. D. Pollard, J. Cell Biol. **106**, 1947 (1988).
[15] S. Anthony, L. Zhang, and S. Granick, Langmuir **22**, 5266 (2006).
[16] W. Wang, H. Pottmann, and Y. Liu, ACM Trans. Graph. **25**, 214 (2006).
[17] C. P. Brangwynne, G. H. Koenderink, E. Barry, Z. Dogic, F. C. MacKintosh, and D. A. Weitz, Biophys. J. **93**, 346 (2007).
[18] J. Käs, H. Strey, J. X. Tang, D. Finger, R. Ezzell, E. Sackmann, and P. A. Janmey, Biophys. J. **70**, 609 (1996).
[19] A. G. Ogston, Trans. Faraday Soc. **54**, 1754 (1958).
[20] D. C. Morse, Phys. Rev. E **63**, 031502 (2001).
[21] M. Tassieri, R. M. L. Evans, L. Barbu-Tudoran, G. N. Khaname, J. Trinick, and T. A. Waigh, Phys. Rev. Lett. **101**, 198301 (2008).
[22] H. Hinsch, J. Wilhelm and J. Frey, Eur. Phys. J. E **24**, 35 (2007).
[23] J. Glaser *et al.*, arXiv:0910.5864.